This article may be downloaded for personal use only. Any other use requires prior permission of the author and AIP Publishing. This article appeared in Lingwei Zeng, T. H. New, Hui Tang; Control of cylinder wake using oscillatory morphing surface. Physics of Fluids 1 May 2024; 36 (5): 057144 and may be found at https://doi.org/10.1063/5.0208868.

RESEARCH ARTICLE | MAY 24 2024

Control of cylinder wake using oscillatory morphing surface

Lingwei Zeng (曾令伟) ; T. H. New ; Hui Tang (唐辉)

Check for updates

Physics of Fluids 36, 057144 (2024)
https://doi.org/10.1063/5.0208868

View Online
Export Citation

11 July 2024 03:57:19

APL Energy
Latest Articles Online!
Read Now
AIP Publishing

Physics of Fluids ARTICLE pubs.aip.org/aip/pof

Control of cylinder wake using oscillatory morphing surface

Cite as: Phys. Fluids **36**, 057144 (2024); doi: 10.1063/5.0208868
Submitted: 17 March 2024 · Accepted: 10 May 2024 ·
Published Online: 24 May 2024

Lingwei Zeng (曾令伟),[1] T. H. New,[2,a)] and Hui Tang (唐辉)[1,a)]

AFFILIATIONS

[1] Department of Mechanical Engineering, The Hong Kong Polytechnic University, Kowloon, Hong Kong, China
[2] School of Mechanical and Aerospace Engineering, Nanyang Technological University, Singapore

[a)] Authors to whom correspondence should be addressed: dthnew@ntu.edu.sg and h.tang@polyu.edu.hk

ABSTRACT

In this study, the wake of a cylinder was actively controlled by the cylinder's oscillatory morphing surface. Experiments were conducted in a closed-loop water channel. A cylinder of diameter 36 mm was placed in 0.09 m/s water flow, resulting in the Reynolds number 3240 and the vortex shedding frequency around 0.5 Hz. The cylinder's morphing surface oscillated at four different frequencies, i.e., 0.5, 1, 2, and 4 Hz. It was found that, compared to the rigid circular cylinder, the cylinder with oscillatory morphing surface can generally produce a smaller vortex formation length, especially at intermediate oscillation frequencies. The shear layers developed from the cylinder transit and roll up earlier due to enhanced flow instabilities. With the highest-frequency oscillations, the shear layer develops into a train of many small vortices that follow the trace of undisturbed shear layer. This study reveals some physical insights into this novel flow control method, which could be useful in future engineering applications.

Published under an exclusive license by AIP Publishing. https://doi.org/10.1063/5.0208868

11 July 2024 03:57:19

I. INTRODUCTION

Bluff bodies are very common in both natural environments and various engineering applications, including, but not limited to, bridges, buildings, and marine structures. Fluid flows around a bluff body can usually lead to various phenomena such as flow separations, vortex formation and shedding, and flow-induced vibrations.[1–3] To control bluff-body wakes, various passive and active flow control technologies have been proposed,[4] such as surface modifications[5–7] and synthetic jets.[8,9] A two-dimensional circular or square cylinder is the most used representative of bluff bodies.[10–14]

Many thought-provoking shape optimizations are inspired by biological living things, including sharks, seashells, and cacti.[15] The present work was motivated by the shape and structural characteristics of cacti, which were found to have better aerodynamic performance and flow behavior in high winds than a plain cylinder.[16–20] For an adult cactus found in nature, the number of grooves along its stem ranges from 10 to 30.[21] The aerodynamic performance of a 24 V-shaped cacti cylinder was first experimentally investigated by Talley *et al.*[20] at the Reynolds number ranging from $Re = 90\,000$ to $200\,000$. Their study revealed that the cacti cylinder can effectively suppress its drag and fluctuating lift as compared to a plain cylinder. This improvement is attributed to the narrower wake and smaller velocity deficit caused by the cacti structure, as well as the three-dimensional flow effects it produces. A similar three-dimensional flow behavior was further reported by Babu and Mahesh[19] on a 24 V-shaped succulent cylinder at $Re = 300$. They found that flow separation occurs early for the succulent cylinder, thus forming a larger recirculation region than a plain cylinder. The primary contributor to drag reduction was identified as the decrease in viscous force, facilitated by the large-scale, quiescent, recirculating flow within the cavities of the cactus. Later, Liu *et al.*[18] and Wang *et al.*[22] experimentally confirmed the larger recirculation region produced by a 24 V-shaped cacti cylinder at $Re = 1500$ and $54\,000$, respectively. Other than the large-scale vortices, they also observed the generation of small vortices in shear layer due to the presence of the cavities. They change the downstream flow in the same phase, leading to a remarkable reduction (up to 50%) in fluctuating forces. However, the studies mentioned above are focused on a succulent-shaped cylinder with a rigid surface.

Only very limited studies have investigated the effects of morphing cacti-shaped surfaces on the resulting flow behavior and aerodynamic performance. For example, Guttag and Reis[23] studied the drag reduction of a morphing cylinder through wind tunnel tests with a steady pneumatic loading at $Re = 25\,000–150\,000$. The morphing was realized by the pressure difference (almost linearly with the cavity depth) generated between the interior and exterior of the cylinder. Different groove numbers ($N = 14$, 16, 20, 24) have also been considered. They reported that a maximum drag reduction of about 55% can be achieved due to an early occurrence of the drag crisis happening for a plain cylinder. In addition, they proposed a model to predict pneumatic loading in achieving minimal drag for a given incoming flow speed and groove depth.

A research question is, therefore, raised from Guttag and Reis' work.[23] What if the morphing surface oscillates and can the surface oscillation achieve better control? To address this question, in this study, we aim to study the effect of surface oscillations on the wake of a 12-grooved cacti cylinder. This paper is organized as follows: In Sec. II, the experimental setup and methodologies are introduced. The effects of oscillatory morphing surface on the resulting flow fields and associated vortex shedding behavior are presented and discussed in Sec. III. A summary is given in Sec. IV.

II. EXPERIMENTAL SETUP AND MEASUREMENTS

The experiments were conducted in a closed-loop water channel with a test section of 0.45 m (W) × 0.6 m (H) × 1.1 m (L). The freestream velocity can be varied between 0.04 and 0.18 m/s, with a turbulence intensity level of less than 1%. For more details, readers can refer to Wen *et al.*[24] and Wei *et al.*[25] A rigid circular (denoted as baseline) cylinder of diameter $D = 36$ mm and length $H = 420$ mm was positioned vertically at the center of the test section, as illustrated in Fig. 1(a), which resulted in a small blockage ratio of 8%. Two flat plates with round leading edges and similar lateral dimensions as the test section were mounted horizontally at the cylinder's two ends to fix the cylinder and to minimize boundary-layer effects. This led to an effective cylinder length of 10D. A membrane-covered cylinder, which consisted of a steel skeleton and longitudinally attached ribs, was also manufactured. Its working diameter remained at 36 mm. The ribs were used to support a latex membrane of 0.5 mm thickness, as shown in Fig. 1(b). The height of the rib and the length of the membrane between two adjacent ribs were 0.15D and 0.27D, respectively. A few holes of diameter 8 mm were drilled through the skeleton along a spiral line on the cylinder surface [see Fig. 1(c)] so as to unify the pressure inside the cylinder. An external oscillating piston was used to push/pull water from the steel skeleton, which led to the deformation of the membrane. Water was enclosed in a circuit consisting of a pipe, a crank slider, and a membrane cylinder. The two ends of the cylinder are also sealed using the membrane to prevent water from exchanging between the inside and outside of the cylinder. Hose clips were used in the connection points to avoid water and air leakages, as depicted in Fig. 1(a).

The freestream velocity was set at $U_\infty = 0.09$ m/s with a resulting Reynolds number of $Re = U_\infty D/\nu = 3240$, where ν is the kinematic viscosity of water. With the Strouhal number of the baseline cylinder being about $St = f_{\mathrm{vor}} D/U_\infty = 0.2$,[26,27] the natural frequency of its vortex shedding was about $f_{\mathrm{vor}} = 0.5$ Hz. To study the effects of surface oscillations, the membrane surface was driven at four different harmonics of the baseline wake frequency, i.e., $f_{\mathrm{osc}} = 0.5$, 1, 2, and 4 Hz. For convenience, we define a dimensionless oscillatory frequency $f^*_{\mathrm{osc}} = f_{\mathrm{osc}}/f_{\mathrm{vor}}$ to describe these oscillations for the cylinder with oscillatory morphing surface, i.e., $f^*_{\mathrm{osc}} = 1$, 2, 4, and 8. For comparison purposes, a rigid circular cylinder and a cylinder covered with non-oscillating membrane are served as the benchmark cases.

A time-resolved particle image velocimetry (TR-PIV) system was used to measure the flow in the near wake of the cylinders. In this system, a 2-W, 532-nm wavelength, continuous-wave laser was used to provide a laser beam. Beam-steering mirrors were used to redirect the laser beam to a plano-concave cylindrical lens that expands the laser beam into a thin laser sheet of approximately 1.5 mm thick, as depicted in Fig. 1(a). The 20 μm tracer particles were used to seed the water flow. A high-speed CCD camera (IDT NX8-S1) was used to capture raw particle images with a resolution of 1600 × 1200 pixels^2. The sampling framerate was 200 frames per second (FPS). A total of 25 000 images (about 62.5 natural vortex-shedding cycles) were recorded to ensure statistical convergence. The exposure time was kept at about 2.5 ms to minimize the streaking of the particles. PIV measurements were conducted in two different measurement windows, with window sizes of 5D and 2D, corresponding to spatial resolutions of 0.1125 and 0.045 mm/pixel, respectively. The larger measurement window was selected for Proper Orthogonal Decomposition (POD) analysis, while the smaller measurement window enabled detailed observations of shear-layer developments.

The PIVlab[28] software was used within MATLAB™ to analyze the raw particle images. The post-processed procedures were similar to those used by New *et al.*[29,30] and New and Zang.[31] Readers may refer to those papers for the data-processing and uncertainty analysis details. To acquire the velocity maps, three interrogation windows and two sets of multi-grid cross correlations were used on the sequential particle images. The initial and final interrogation windows were 128 × 128 and 32 × 32 pixels^2, respectively, with 50% overlap in both directions. The experimental uncertainty for the present velocity map (99 × 74 vectors) was estimated to be less than 2%.

POD is a mathematical technique used for data analysis and signal processing. It is a method for decomposing a signal or dataset into a set of orthogonal basis functions, which are ranked according to their contribution toward the total variance in the data. This allows for a simplified representation of complex datasets, where only the most significant basis functions are retained. Based on the snapshot POD technique,[32–35] dominant flow structures can be differentiated by decomposing the velocity fields into individual modes, which would help to better understand the underlying flow physics under different surface oscillations. To do that, the TR-PIV measured velocities are first decomposed into the mean and fluctuating velocity components, with the latter being further decomposed into various POD modes. The POD modes are then ranked according to their energy contributions. Motivated by New *et al.*,[33,34] the phase-averaged results were also reconstructed by averaging the PIV data in $\pi/3$ intervals with a $\pm\pi/72$ phase bin size. This is possible due to the highly cyclical nature of the vortex shedding behavior observed for the present test cylinders.

III. RESULTS AND DISCUSSION

A. Evolution of oscillatory morphing surface

The deformation of the membrane was measured using a thin laser sheet by tracing the membrane outline and imaged using a high-speed camera. The oscillatory displacement y^* ($= y/D$) was obtained at the midpoint of the membrane section between two neighboring ribs and averaged over four such membrane sections. In this study, normalization by D and/or U_∞ is denoted with a superscript "$*$." As revealed in Fig. 2, the variation of y^* under excitation of all four frequencies is highly periodic. For all tested cases, their oscillation amplitude is approximately 0.0065D (0.234 mm). The ratio of this amplitude to the length of membrane section is about 2.4%. In addition, the peak

11 July 2024 03:57:19

Published under an exclusive license by AIP Publishing

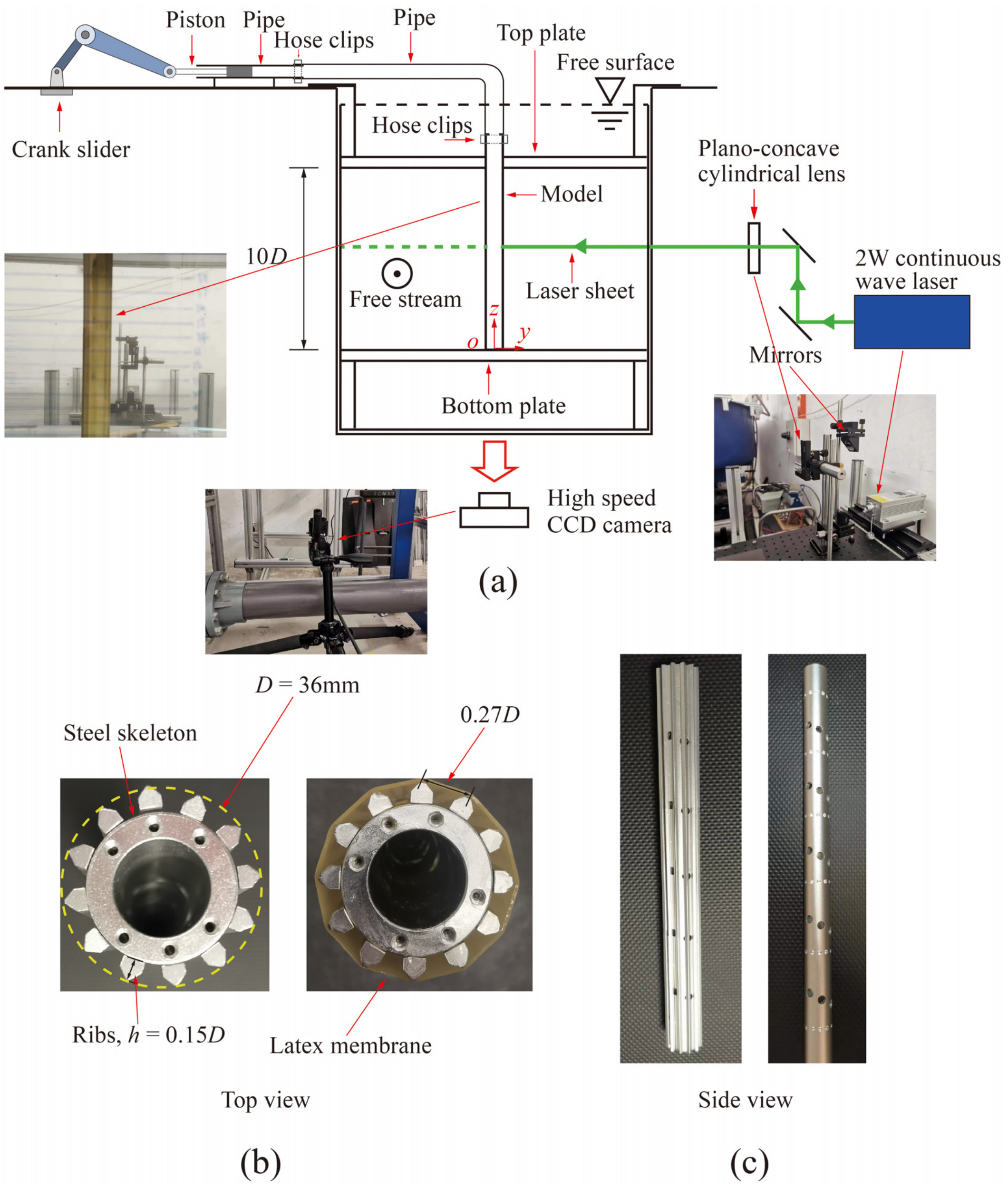

FIG. 1. (a) Schematics of the experimental setup and water tunnel; (b) cross sections of the experiment model with and without latex membrane wrapped around it as viewed from the top and (c) side-view of the steel cylindrical skeleton with (left) and without (right) ribs.

displacements under oscillations of different frequencies are close as the stroke length of the crank slider is identical.

As an example, the snapshots of oscillatory morphing surfaces at selected instants (t_1–t_5) over half an excitation cycle for the morphing-surface cylinder oscillating at $f^*_{\mathrm{osc}} = 2$ are given at the bottom of Fig. 2. The shrinking and expanding membrane interact with the incoming flow, which may affect the flow separation and the stability of the generated shear layers.

B. Effects on vortex shedding

Figure 3 compares the vortex shedding processes behind the rigid circular (RC) cylinder, the grooved, static surface (SS) cylinder, and the grooved, oscillatory morphing surface (OMS) cylinder driven at $f^*_{\mathrm{osc}} = 1$, 2, 4, 8. For the RC and SS cylinders, the elongated shear layers can be clearly seen (compared with the OMS cylinders driven at $f^*_{\mathrm{osc}} = 2$, 4, and 8), which roll up into large vortices as shown in Figs. 3(a) and 3(b), resembling the observation reported by El-Makdah and Oweis.[17]

11 July 2024 03:57:19

Published under an exclusive license by AIP Publishing

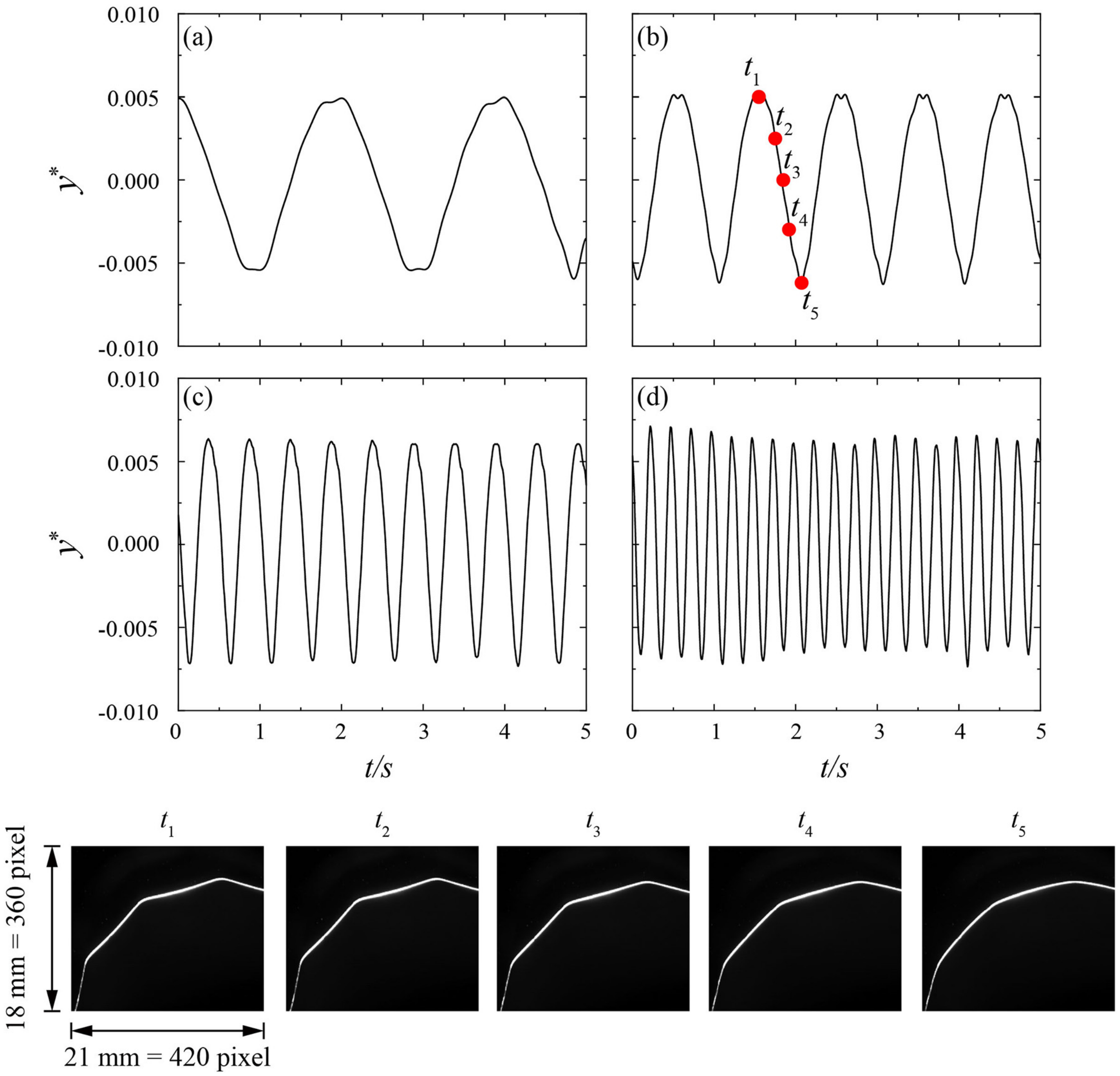

FIG. 2. Averaged deformation of oscillatory morphing surfaces at different excitation frequencies: (a) oscillatory morphing surface (OMS) cylinder at $f^*_{\mathrm{osc}} = 1$; (b) OMS cylinder at $f^*_{\mathrm{osc}} = 2$; (c) OMS cylinder at $f^*_{\mathrm{osc}} = 4$; and (d) OMS cylinder at $f^*_{\mathrm{osc}} = 8$. Snapshots of oscillatory morphing surfaces at different instants (t_1–t_5) over half an excitation cycle for OMS cylinder at $f^*_{\mathrm{osc}} = 2$ are given at the bottom position.

The small vortices shown in the instantaneous flow fields may be caused by turbulence related to the subcritical flow at the present Reynolds number. The rolling-up of the shear layers from the SS cylinder is slightly later than that from the RC cylinder, possibly due to early flow separation caused by the ribs of the SS cylinder, as sketched in Fig. 4(b). For the OMS cylinder at $f^*_{\mathrm{osc}} = 1$, its shear layers roll up slightly early and thus may exhibit a shorter vortex formation length [Fig. 3(c)].

As the excitation frequency increases, i.e., the OMS cylinder at $f^*_{\mathrm{osc}} = 2$ and 4, the interaction between the membranes and the shear layers becomes stronger, thus breaking the integrity and continuity of the shear layers, as shown in Figs. 3(d) and 3(e). As such, the rolling-up of the shear layers occurs significantly earlier, leading to a significantly shorter vortex formation length as will be revealed in Fig. 8 later.

Interestingly, at the highest driving frequency $f^*_{\mathrm{osc}} = 8$, the broken-up shear layers grow into many small vortices that still follow the trace of the primary shear layers, as shown in Fig. 3(f). This wake pattern is quite similar to that obtained by Wang *et al.*[8] and Ma and Feng[36] using synthetic jets operating at high perturbation frequencies. These small vortices then roll up like the primary shear layers to form the von Karman vortex street. As such, both the dominant vortex shedding frequency ($f^* = f/f_{\mathrm{vor}} = 0.9$) and the excitation frequency ($f^* = 7.2$) are prominent in the spectra presented in Fig. 5(f). The well-organized small vortices along the trace of the primary shear layers are almost parallel, reflecting significantly weaker interactions between the

11 July 2024 03:57:19

Published under an exclusive license by AIP Publishing

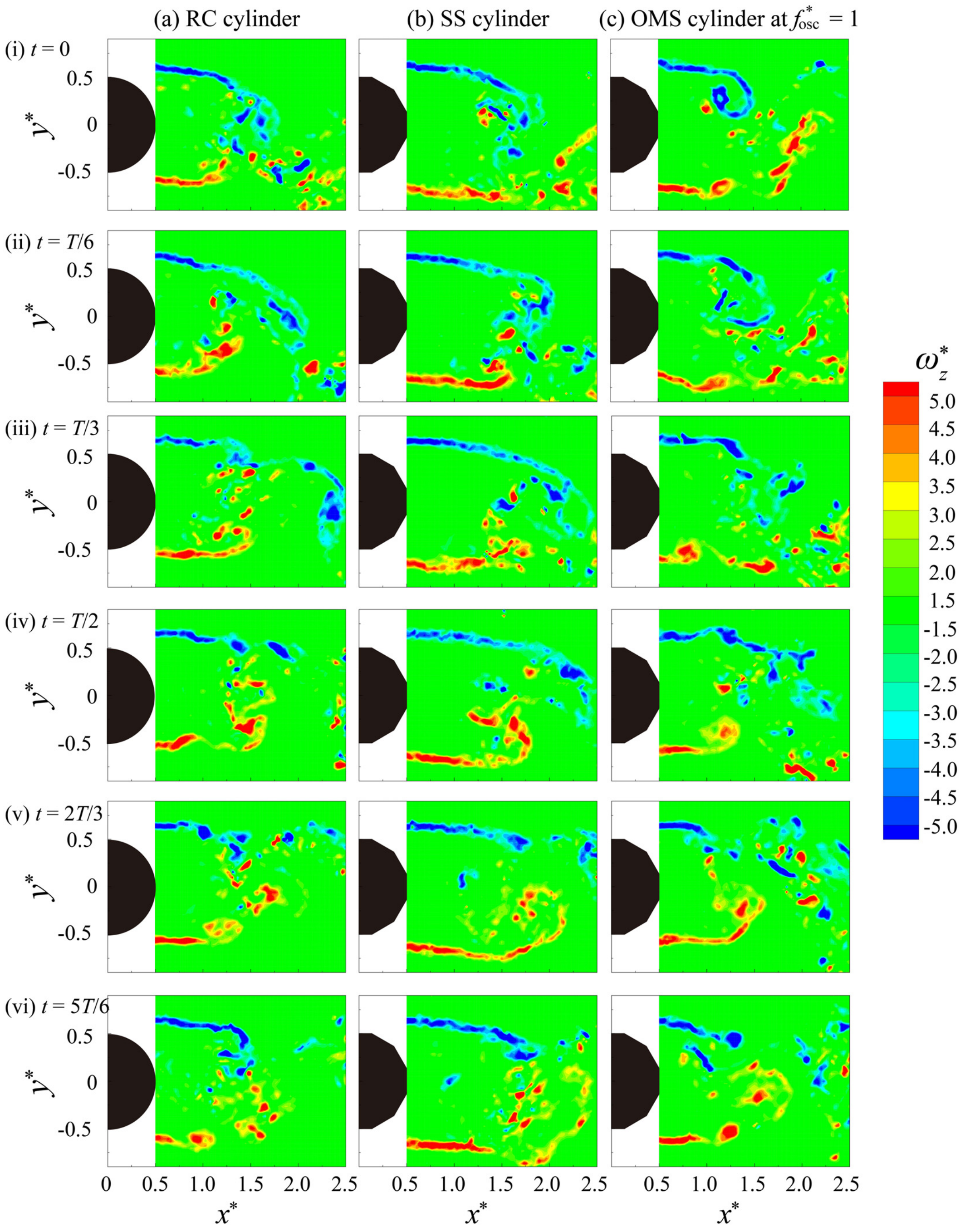

FIG. 3. Instantaneous spanwise vorticity ω_z^* for the (a) RC cylinder, (b) SS cylinder, (c) OMS cylinder at $f^*_{osc} = 1$, (d) OMS cylinder at $f^*_{osc} = 2$, (e) OMS cylinder at $f^*_{osc} = 4$, and (f) OMS cylinder at $f^*_{osc} = 8$, where (i) $t = 0$, (ii) $t = T/6$, (iii) $t = T/3$, (iv) $t = T/2$, (v) $2T/3$, and (vi) $5T/6$ are the different periods in one vortex shedding cycle.

opposite-signed vortices as compared to the RC and SS cases. These observations also indicate that an excitation frequency close to the natural vortex-shedding frequency may not significantly change its vortex-shedding behavior.

To summarize our observations, we sketch in Fig. 4 different vortex patterns for the RC and SS cylinders, as well as the OMS cylinder at $f^*_{osc} = 2$ and 8. For the RC cylinder, flow separation occurs at a location slightly larger than 90° (0° is defined as the upstream stagnation

11 July 2024 03:57:19

Published under an exclusive license by AIP Publishing

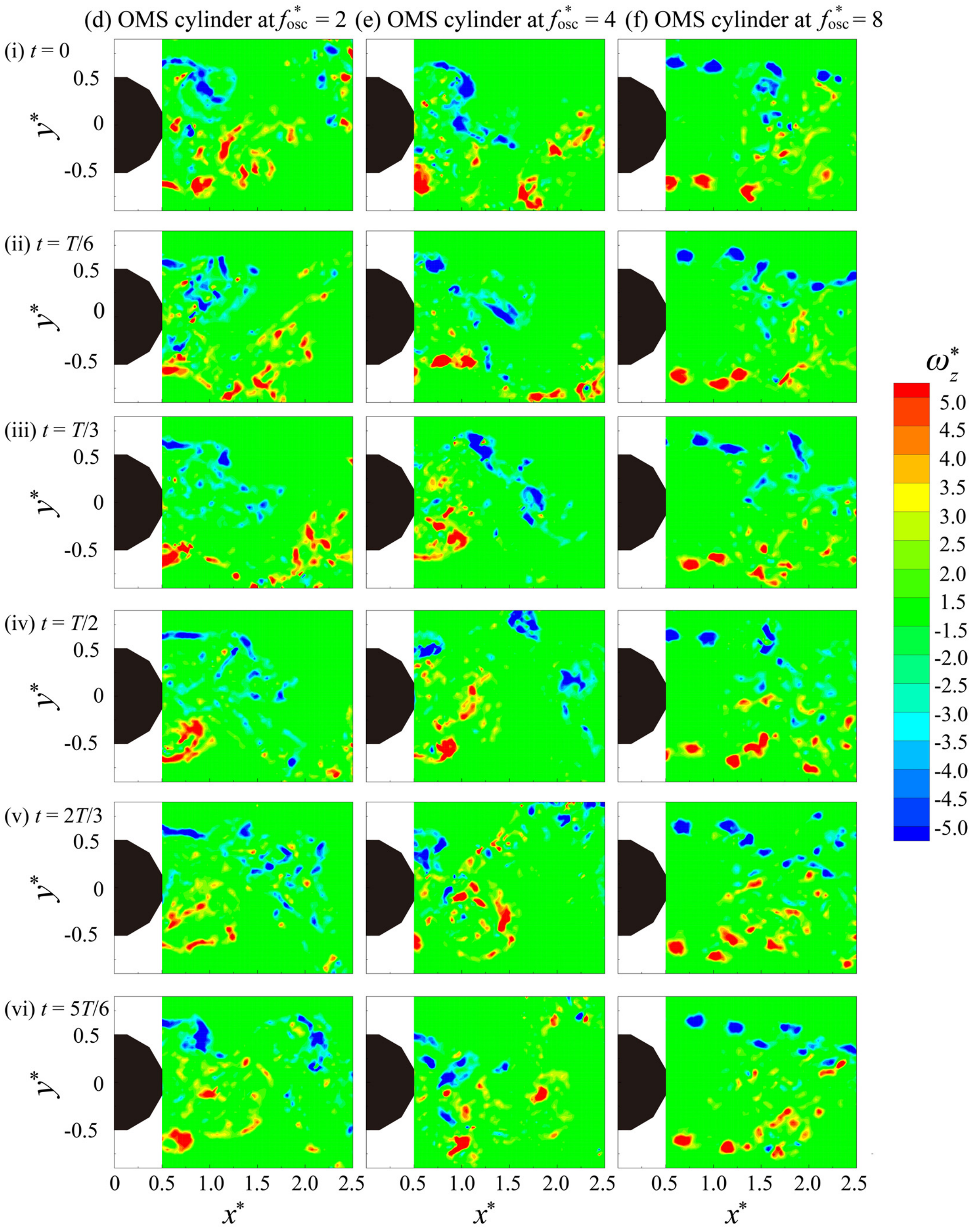

FIG. 3. (*Continued.*)

11 July 2024 03:57:19

point) due to turbulence associated with the subcritical flow,[37] and a classical von Karman vortex street forms in the wake [Fig. 4(a)]. In contrast, the SS cylinder shows early separation caused by the rib right before 90°, leading to the formation of a wider and longer wake, as sketched in Fig. 4(b). Note that the separation points in these sketches are qualitatively determined based on the cylinder's geometric features and our observations, especially the initial locations and directions of the two shear layers, from the instantaneous flow fields as presented in Fig. 3.

For the OMS cylinder, the oscillatory morphing surface delays the occurrence of flow separation, and meanwhile increases the instability of the separated shear layers, leading to an early rolling-up.

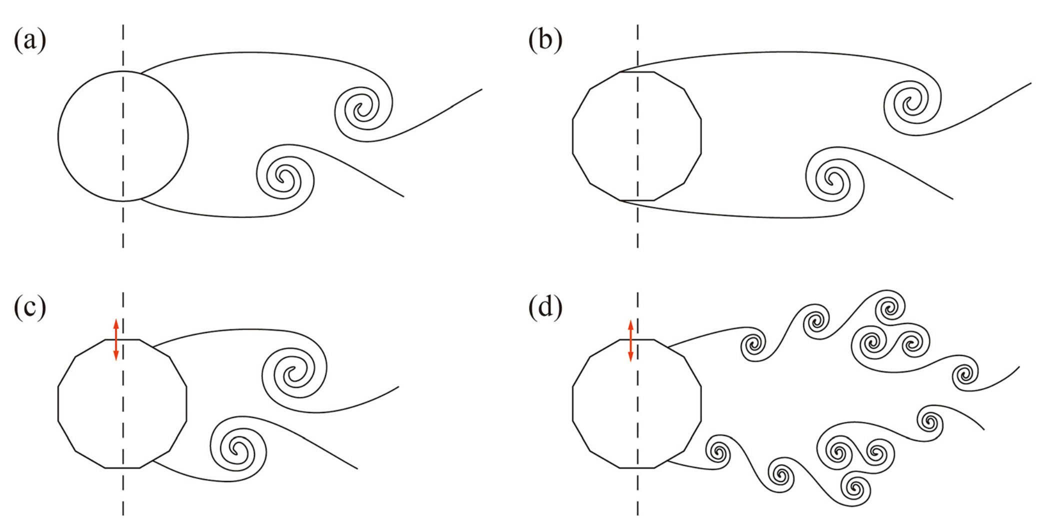

FIG. 4. Schematics of the vortex street for the (a) RC cylinder, (b) SS cylinder, (c) OMS cylinder at $f^*_{osc} = 2$, and (d) OMS cylinder at $f^*_{osc} = 8$. The red arrow denotes the oscillating of the morphing surface.

As such, a shorter and narrower wake will form [Fig. 4(c)]. Moreover, when the excitation frequency is as high as $f^*_{osc} = 8$, small vortices are induced along the trace of the primary shear layers. Although disturbed by the small vortices, the primary shear layers can still roll up into large vortices, forming a unique flow pattern as sketched in Fig. 4(d).

Power-spectral-density (PSD) analysis is also conducted for the wakes, as presented in Fig. 5, on the cross-stream velocities at two selected locations, i.e., point A: $x^* = 1.0$, $y^* = 0.5$, and point B: $x^* = 1.5$, $y^* = 0.5$ [denoted in Fig. 5(a)], with all 25 000 velocity maps. These two probe locations are selected to detect the evolution of shear layers and the resulting vortex-shedding behavior. The PSD was determined

11 July 2024 03:57:19

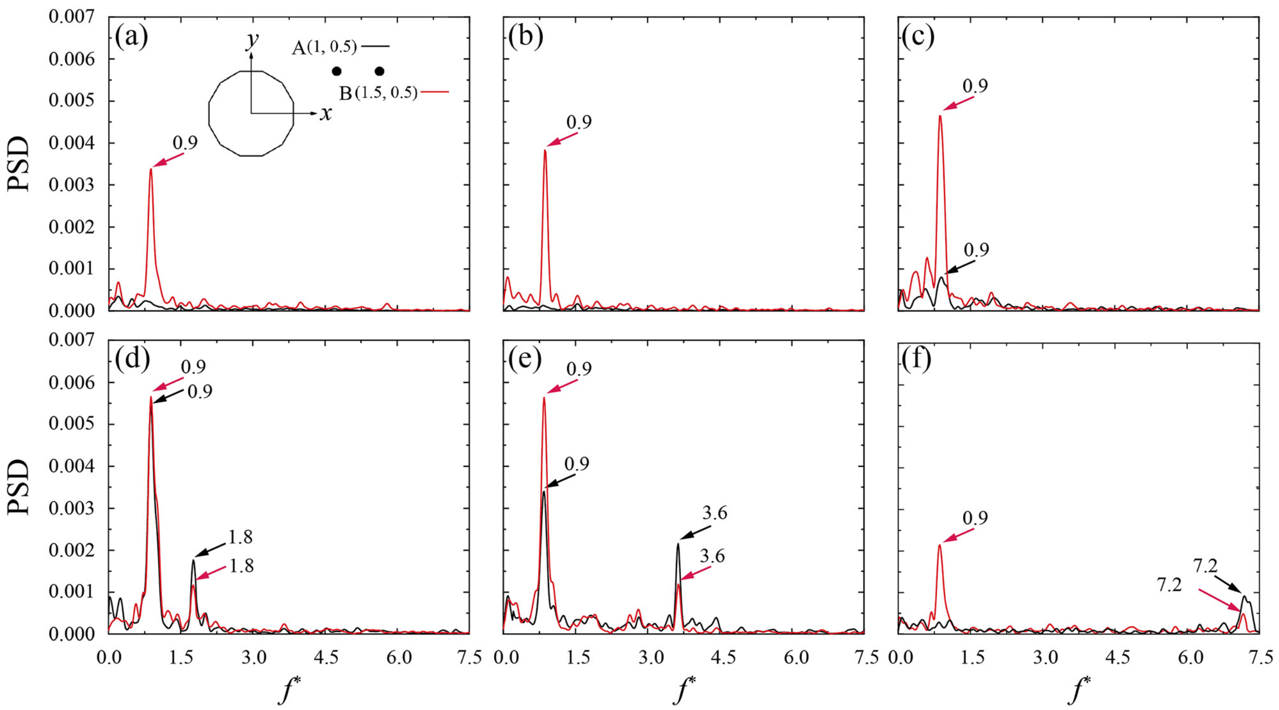

FIG. 5. Power-spectral-density (PSD) analysis for the cross-stream velocities v at point A ($x^* = 1.0$, $y^* = 0.5$) and point B ($x^* = 1.5$, $y^* = 0.5$): (a) RC cylinder; (b) SS cylinder; (c) OMS cylinder at $f^*_{osc} = 1$; (d) OMS cylinder at $f^*_{osc} = 2$; (e) OMS cylinder at $f^*_{osc} = 4$; and (f) OMS cylinder at $f^*_{osc} = 8$.

Published under an exclusive license by AIP Publishing

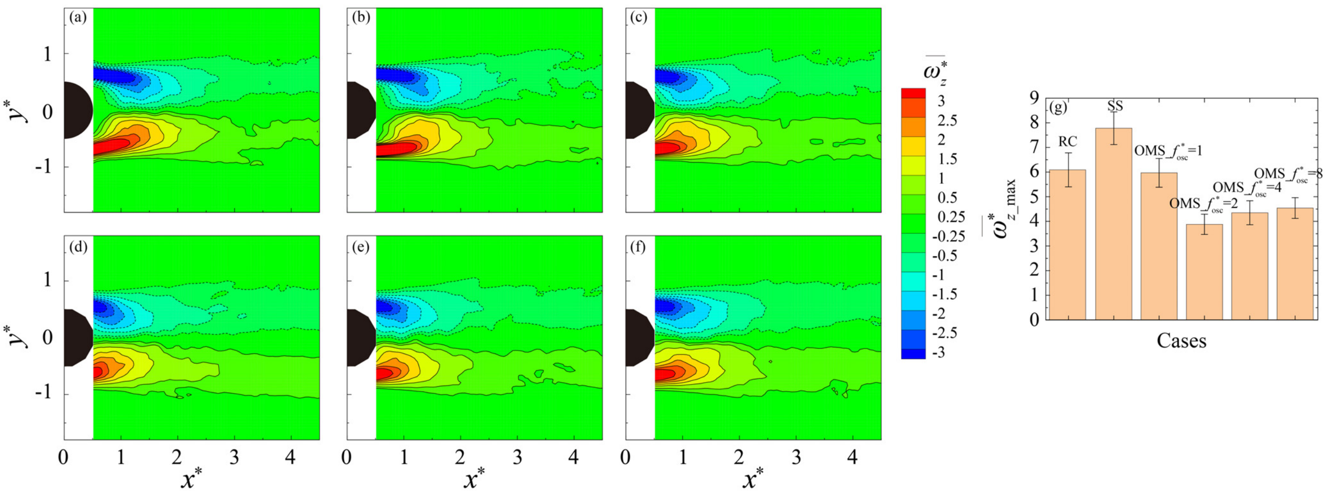

FIG. 6. Distribution of mean vorticity $\overline{\omega_z^*}$ in the near wake of cylinders with different perturbations: (a) RC cylinder; (b) SS cylinder; (c) OMS cylinder at $f^*_{osc} = 1$; (d) OMS cylinder at $f^*_{osc} = 2$; (e) OMS cylinder at $f^*_{osc} = 4$; and (f) OMS cylinder at $f^*_{osc} = 8$. The local maximum vorticity of the cylinders with different frequency excitations is compared in (g).

using the MATLAB *pwelch* function with a segment length of 5000 and a Hamming window with 50% overlap. As revealed in Figs. 5(a) and 5(b), no evident dominant frequency is detected at point A for the RC and SS cylinders, indicating that the rolling-up of the shear layers does not occur at this location. This is not surprising because the RC and SS cylinders have a longer vortex formation length, and the probe location is within the recirculation region. This observation is consistent with the instantaneous flow structures shown in Figs. 3(a) and 3(b). In contrast, a dominant peak appears at $f^* = 0.9$ for the OMS cylinder driven at $f^*_{osc} = 2$ and $f^*_{osc} = 4$, as shown in Figs. 5(d) and 5(e), corresponding to the vortex shedding frequency. Note that the detected vortex shedding frequency is $f^* = 0.9$, corresponding to 0.45 Hz that is slightly less than the estimated 0.5 Hz. Since these two frequencies are still very close, lock-in phenomena occur as confirmed in Fig. 5. Hence, the oscillation frequencies we applied can promote or mitigate the fundamental wake shedding frequency and its harmonics. The oscillation frequency of the morphing surface also appears in these two cases, although it has a weaker PSD magnitude. This indicates that the vortex shedding occurs closer to the cylinder, which agrees well with that observed in Fig. 3. In addition, the vortex shedding frequency is not attracted to the excitation frequencies that are the former's even multiples, implying that the lock-on phenomenon as reported by Wang *et al.*[38] does not occur here. The reason is probably that the membrane oscillations are still not strong enough to induce the attraction. At the other two excitation frequencies, i.e., the lowest one $f^*_{osc} = 1$ and the highest one $f^*_{osc} = 8$, only a weak peak is observed at the excitation frequency, as shown in Figs. 5(c) and 5(f), suggesting that the roll-up of shear layers is almost not affected by the weak excitation.

As the probe moves downstream to point B, the dominant vortex shedding frequency can be well captured for the RC and SS cylinders [Figs. 5(a) and 5(b)]. The peak for the SS cylinder (0.0039) is also slightly higher than that for the RC cylinder (0.0034), indicating that the SS cylinder generates stronger vortex shedding. This is consistent with the vorticity information revealed in Fig. 6. After applying the excitation, the energy at the dominant vortex shedding frequency is significantly enhanced in the $f^*_{osc} = 1$, 2, and 4 cases. Additionally, the peaks at the excitation frequency in the $f^*_{osc} = 2$ and 4 cases are lower than their counterparts at point A, showing the decaying feature of the excitation influence.

C. Effects on mean flow field

Figure 7 shows the influence of oscillatory morphing surface on the time-averaged flow fields, including the streamwise ($\overline{u}/U_\infty$) and cross-stream ($\overline{v}/U_\infty$) velocities. Compared with the RC and SS cylinders, a narrower wake with a shorter and weaker reversed flow is formed behind the OMS cylinder at $f^*_{osc} = 2$ and 4 [see Figs. 7(c1) and 7(d1)], reflecting the delayed flow separation, which further results in the vortex patterns presented in Figs. 3(a) and 3(b) and sketched in Fig. 4(c). This observation is consistent with the cross-stream velocity contours, in which the peaks for the OMS cylinder at $f^*_{osc} = 2$ and 4 remarkably shift toward the upstream, i.e., closer to the cylinder [Figs. 7(d2) and 7(e2)], suggesting an early roll-up of the shear layers. However, this effect seems to be weakened at the higher frequency, i.e., $f^*_{osc} = 8$ [Figs. 7(f1) and 7(f2)]. In this case, the shear layer is broken up by high-frequency force into a train of small vortices. Although following the trace of the shear layer to roll up [see Fig. 4(d)], the generation of these small vortices attenuates the strength of the shear layer and hence delays the roll-up process.

The contours of time-averaged vorticity shown in Figs. 6(a)–6(f) and the peak vorticity values compared in Fig. 6(g) further revealed that the surface oscillation not only promotes the roll-up of the shear layer but also suppresses its strength, especially for the OMS cylinder at $f^*_{osc} = 2$ and 4. However, without dynamic oscillation, the strength of the shear layer is enhanced, which can be read by comparing vorticities between the SS cylinder case and the RC cylinder case.

Vortex formation length, defined as the distance between the center of the cylinder and the location of zero mean streamwise velocity in the cylinder's centerline, is a key indicator to evaluate the flow behavior

11 July 2024 03:57:19

Published under an exclusive license by AIP Publishing

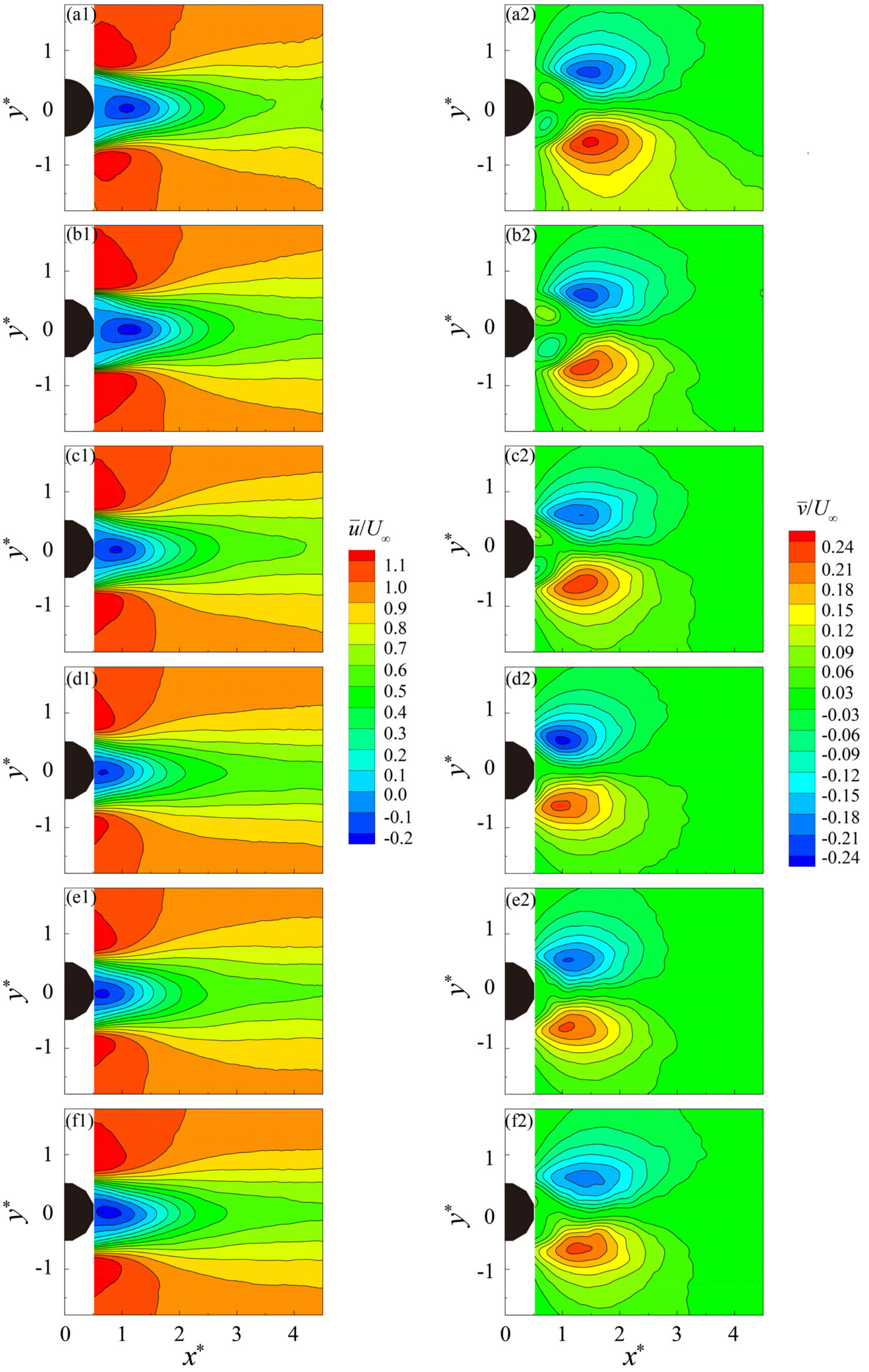

FIG. 7. Variations of mean velocity fields in streamwise direction ($\bar{u}/U_\infty$) and cross-stream direction ($\bar{v}/U_\infty$) around the cylinders with different perturbations: (a1) and (a2) RC cylinder; (b1) and (b2) SS cylinder; (c1) and (c2) OMS cylinder at $f^*_{\mathrm{osc}} = 1$; (d1) and (d2) OMS cylinder at $f^*_{\mathrm{osc}} = 2$; (e1) and (e2) OMS cylinder at $f^*_{\mathrm{osc}} = 4$; and (f1) and (f2) OMS cylinder at $f^*_{\mathrm{osc}} = 8$.

11 July 2024 03:57:19

Published under an exclusive license by AIP Publishing

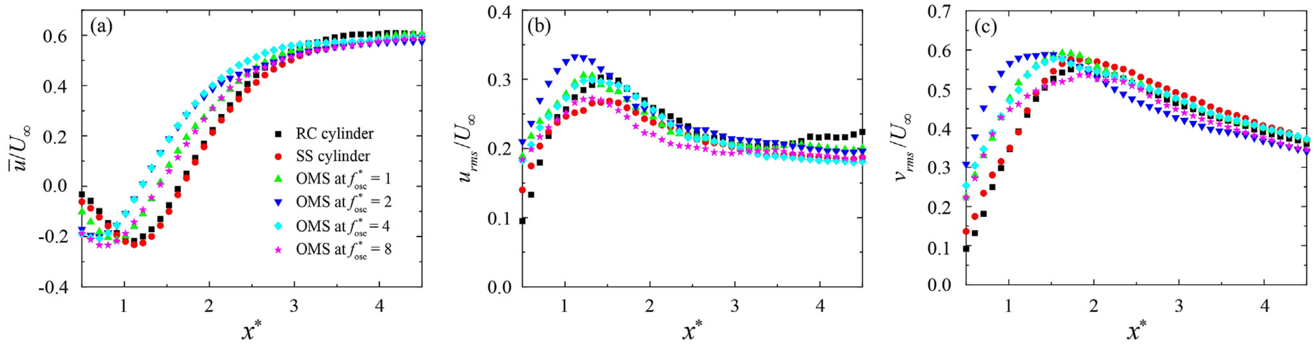

FIG. 8. Distributions of (a) time-averaged streamwise velocities $\overline{u}/U_\infty$; (b) streamwise fluctuating velocity u_{rms}/U_∞, and (c) cross-stream fluctuating velocity v_{rms}/U_∞ in the centerline of cylinders ($y^* = 0$).

(i.e., vortex development and shedding) and aero/hydrodynamic performance (such as base pressure and mean drag) of bluff bodies.[27,33,34,39] The variations of mean streamwise velocities $\overline{u}/U_\infty$ along the centerline (i.e., $y^* = 0$) are compared in Fig. 8(a). It is seen that the vortex formation length for the SS cylinder (1.68*D*) is only slightly longer than that for the RC cylinder (1.63*D*), suggesting that these two cases share similar flow behavior in the near wake, as confirmed by the contours in Figs. 7(a1)–7(b2). This observation aligns with the findings reported by El-Makdah and Oweis,[17] who reported that both circular and cactus-like cylinders exhibit similar characteristics in terms of the magnitudes and spatial extent of the mean streamwise velocity contours at $Re = 50\,000$.

Compared to the RC cylinder, the OMS cylinder results in a smaller vortex formation length, especially at intermediate frequencies of $f^*_{osc} = 2$ and 4. The maximum reduction in vortex formation length of about 25.2% is achieved at $f^*_{osc} = 2$. This observation implies that in these two cases, the rolling-up of shear layers happens closer to the cylinder, which is consistent with the observations in Fig. 3. With perturbations of lower ($f^*_{osc} = 1$) or higher ($f^*_{osc} = 8$) frequencies, however, the vortex formation length turns to increase toward the value of the non-morphing cases, as displayed in Fig. 8(a) as well as in Fig. 7. According to the vortex formation length, it is estimated that the drag experienced by the cylinder is either increased or almost unchanged. The reason for not achieving drag reduction is probably due to the relatively weak oscillatory forcing we applied in the experiments, which is limited by the present experimental setup.

Figures 8(b) and 8(c) show the centerline distribution of the streamwise velocity fluctuation (u_{rms}/U_∞) and cross-stream fluctuation (v_{rms}/U_∞). Compared with the RC cylinder, the streamwise velocity fluctuation for the SS cylinder is slightly stronger in the very near wake, i.e., $x^* < 1$, but becomes obviously weaker downstream. This is not surprising because the rib-supported leading edges of the top and bottom pieces of membranes for the SS cylinder promote earlier flow separation. As such, the shear layers start earlier and also roll up a bit

11 July 2024 03:57:19

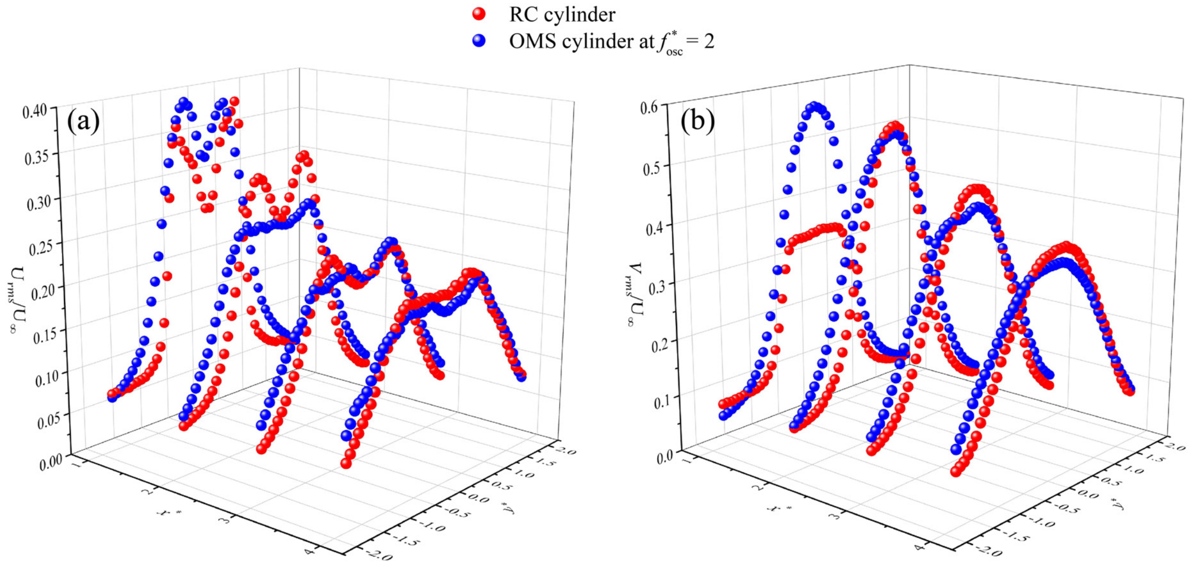

FIG. 9. Distributions of (a) streamwise fluctuating velocity u_{rms}/U_∞ and (b) cross-stream fluctuating velocity v_{rms}/U_∞ along the lines of $x^* = 1$, 2, 3, and 4. The comparison is between the RC cylinder and the OMS cylinder at $f^*_{osc} = 2$.

Published under an exclusive license by AIP Publishing

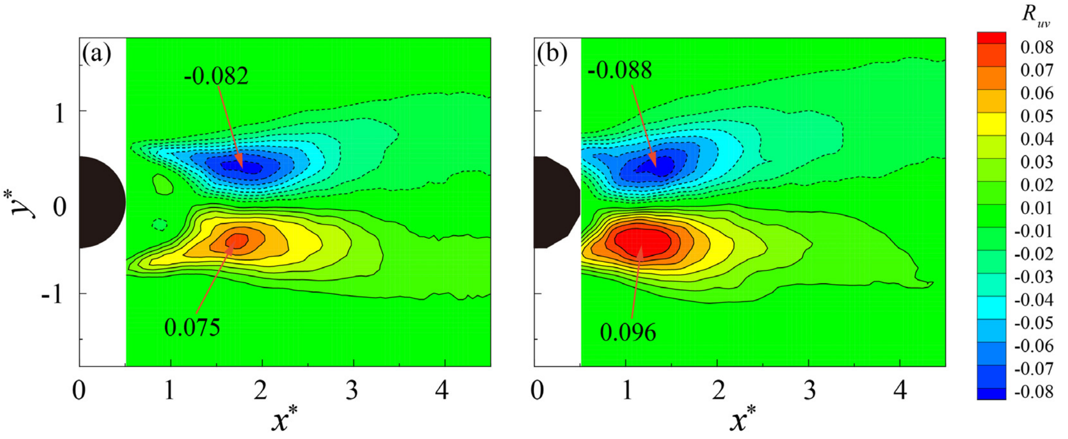

FIG. 10. Distributions of Reynolds shear stress R_{uv} in the near wake of the (a) RC cylinder and (b) OMS cylinder at $f^*_{\text{osc}} = 2$. The local maximum value of R_{uv} is marked in the figure.

earlier, resulting in nearer occurrence of strong streamwise velocity fluctuations. It is also seen that the v_{rms}/U_∞ magnitude for the SS cylinder is slightly larger than the RC cylinder [Fig. 8(b)].

For the OMS cylinder at $f^*_{\text{osc}} = 2$, its velocity fluctuation is significantly stronger with a most upstream peak, indicating that the oscillation of the morphing surface at this frequency promotes earlier roll-up of the shear layers and induces stronger turbulence, as shown in Figs. 8(b) and 8(c). This also leads to a shorter vortex formation length as revealed in Fig. 8(a).

Figure 9 compares u_{rms}/U_∞ and v_{rms}/U_∞ along the $x^* = 1$, 2, 3, and 4 lines between the RC and OMS cylinders at $f^*_{\text{osc}} = 2$. The OMS cylinder at $f^*_{\text{osc}} = 2$ exhibits a significantly greater velocity fluctuation than the RC cylinder at $x^* = 1$, particularly in v_{rms}/U_∞. However, further downstream, the peaks of the u_{rms}/U_∞ and v_{rms}/U_∞ for the RC cylinder are slightly higher than those of the OMS cylinder. It is also observed that the OMS cylinder displays higher velocity fluctuations at locations away from the central line ($y^* = 0$). These findings suggest that the oscillation of the morphing surface enhances the turbulence in the near wake, particularly at $x^* \leq 1$.

To further compare the turbulence effect caused by the OMS cylinder, a comparison has been made on the Reynolds shear stress R_{uv} ($=\overline{u'v'}$) between the RC cylinder and the OMS cylinder driven at $f^*_{\text{osc}} = 2$, as shown in Fig. 10, where u' and v' denote the fluctuation components of u and v, respectively. This quantity is obtained through analyzing all 25 000 instantaneous images. Two observations can be noticed: first, the peak of R_{uv} occurs closer to the cylinder for the OMS

11 July 2024 03:57:19

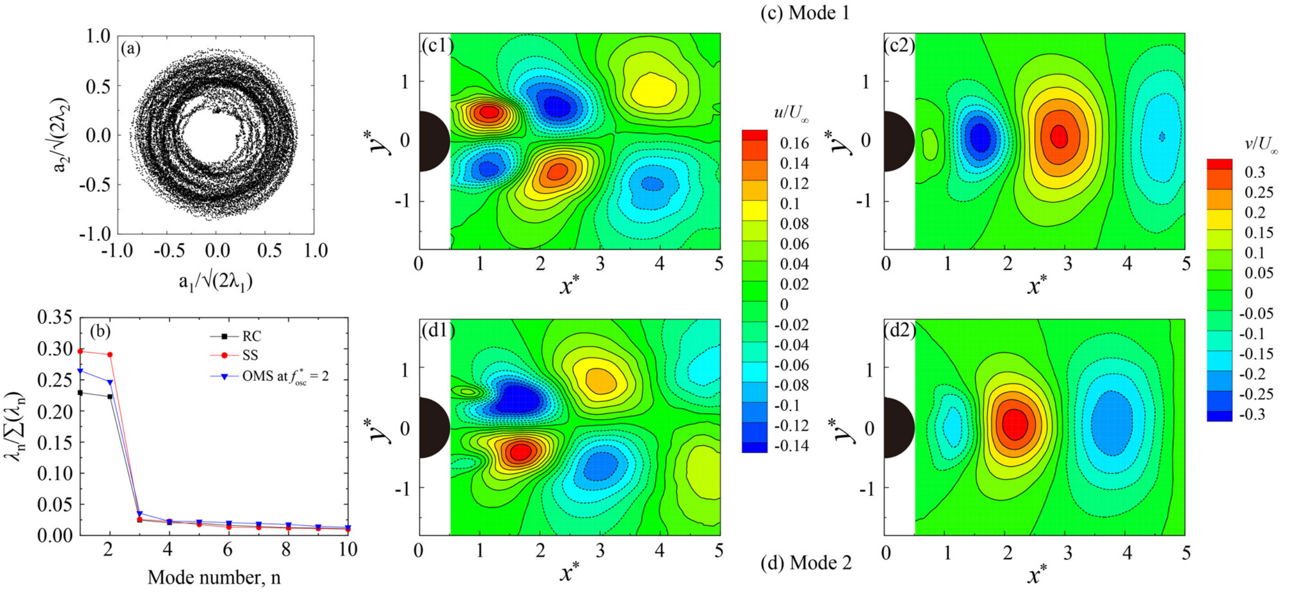

FIG. 11. (a) Coefficient correlations for RC cylinder; (b) POD eigenvalue spectra for the RC cylinder, SS cylinder, and OMS cylinder at $f^*_{\text{osc}} = 2$; and (c) mode 1 and (d) mode 2 distributions for the RC cylinder.

Published under an exclusive license by AIP Publishing

cylinder at $f^*_{osc} = 2$; and second, the absolute maximal value of R_{uv}, which indicates the intensity of interaction between positive and negative vortices, is significantly higher for the OMS cylinder at $f^*_{osc} = 2$ than the RC cylinder. As such, the turbulence intensity near the cylinder is enhanced due to the interaction between the oscillating membranes and the shear layers, which, in turn, alters the near-wake flow structures.

D. POD analysis

In Secs. III A–III C, we have presented and discussed the difference in the mean and instantaneous wakes under different perturbation conditions, which can be attributed to the change of shear layer behavior due to the dynamic morphing. To reveal more physical insights, POD analyses are conducted to extract energy-carrying coherent structures from phase-averaged wakes. Readers can refer to related references for details about the classical Snapshot POD algorithm.[35,40]

Since all the dynamic morphing cases exhibit similar results, for the sake of simplicity, only the RC cylinder, the SS cylinder, and the OMS cylinder at $f^*_{osc} = 2$ are presented and discussed here. Figure 11(a) presents a phase diagram spanned by the coefficients of the first two POD modes, i.e., a_1 and a_2, of the wake of the RC cylinder. It is seen that the (a_1, a_2) point travels in circles, with each circle representing a vortex-shedding cycle. This reflects the good periodicity of the vortex-shedding process and is well suited for phase-averaging analysis.[34,41] Figure 11(b) shows the fractional contributions of the first ten POD modes to the total fluctuation kinetic energy, where λ_n is the eigenvalue of the nth mode. It is seen that the first two modes contribute the most as compared with the other modes for all selected cylinders. This implies that the wake dynamics have not been substantially changed by the dynamic morphing. The energy contribution from the first two modes of the static membrane is higher than the baseline cylinder, which is aligned with the findings of Wang *et al.* on a grooved cylinder.[22]

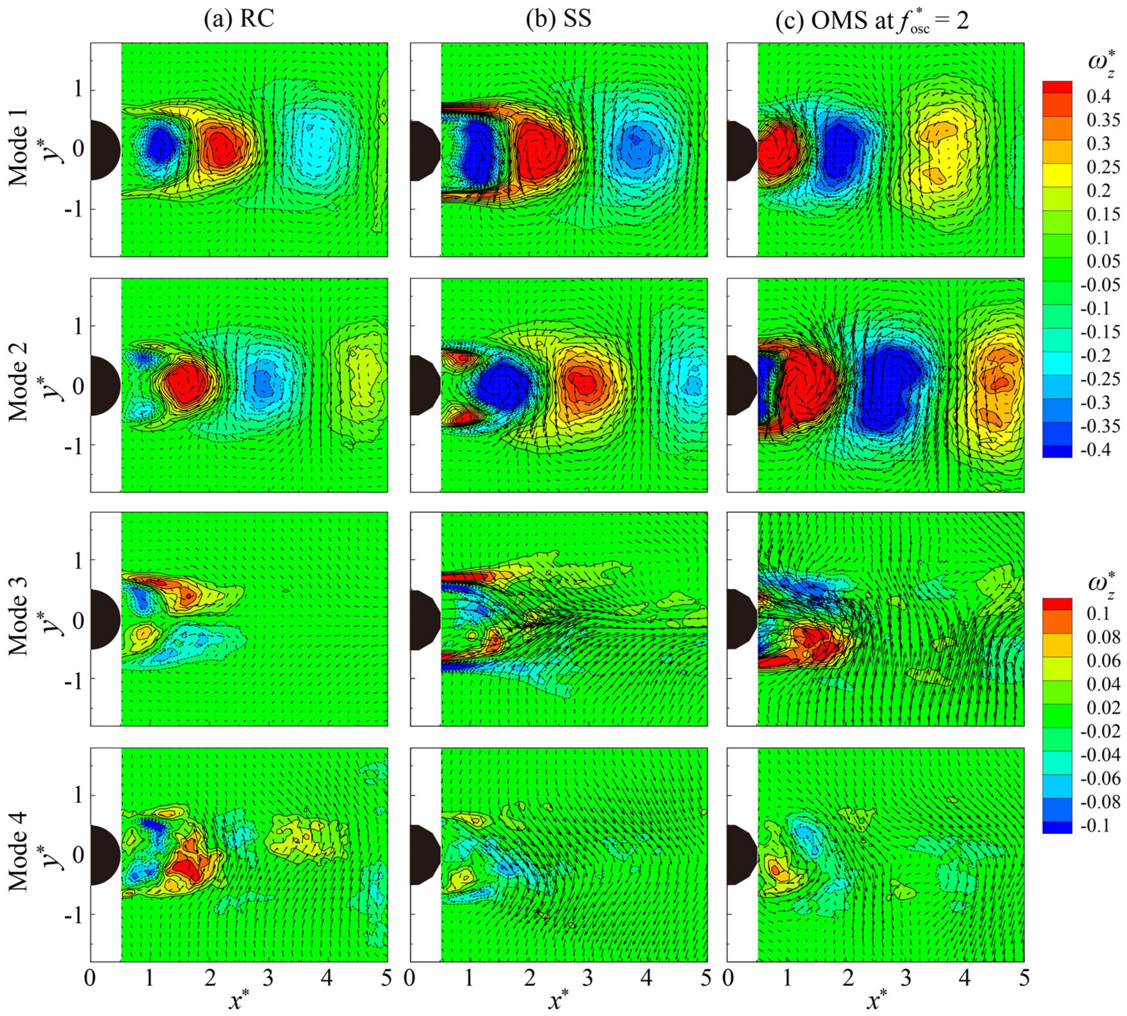

FIG. 12. The ω_z^* contours and velocity vectors of POD modes 1–4 for the selected cases: (a) RC cylinder, (b) SS cylinder, and (c) OMS cylinder at $f^*_{osc} = 2$. The range of ω_z^* for modes 1–2 is −0.4 to 0.4, and the range of ω_z^* for modes 3–4 is −0.1 to 0.1. To better show the vortex structures, the vector scale used in modes 3–4 is different from that used in modes 1–2.

11 July 2024 03:57:19

Published under an exclusive license by AIP Publishing

The u/U_∞ and v/U_∞ contours in the first two POD modes of the RC cylinder are depicted in Figs. 11(c) and 11(d). The u/U_∞ and v/U_∞ data reveal that the vortex-shedding behavior for the captured cases exhibited a high degree of symmetry and repeatability. Modes 1 and 2 exhibit a strong correlation, with about 1/4 cycle streamwise dislocation between them, which is evidenced by the similar mode shapes shown in Figs. 11(c) and 11(d) and the streamwise shift of their u/U_∞ or v/U_∞ peaks. This correlation reflects the evolution of Karman vortex shedding.

To provide a deeper understanding of the flow behavior associated with the oscillatory morphing surface, Fig. 12 presents the flow fields of POD modes 1–4. These are depicted through velocity vectors and vorticity contours. For the RC cylinder, owing to the dominance of energy contribution by the first two modes, the strength of

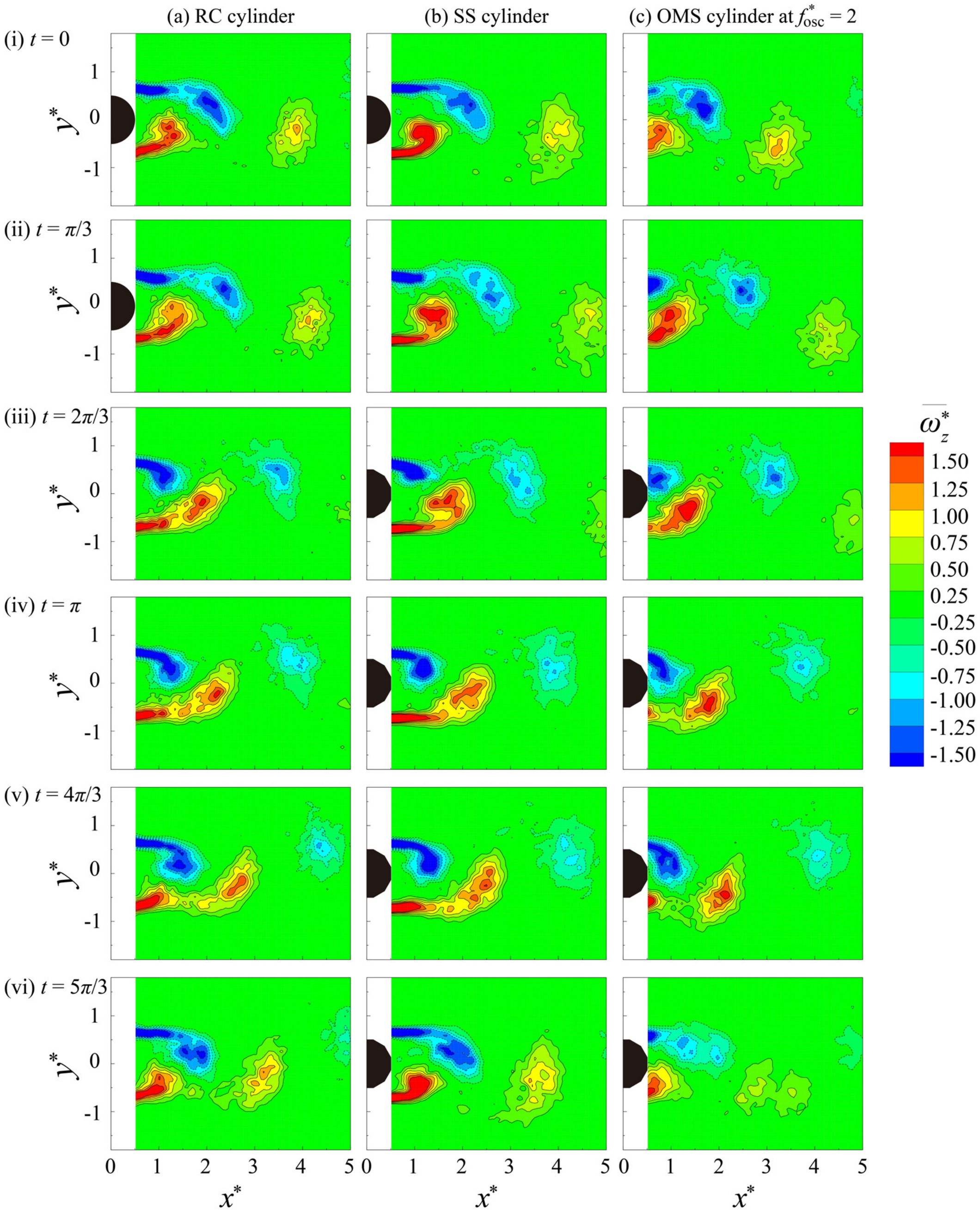

FIG. 13. Phase-averaged results for the (a) RC cylinder, (b) SS cylinder, and (c) OMS cylinder at $f^*_{osc} = 2$, where (i) $t = 0$, (ii) $t = \pi/3$, (iii) $t = 2\pi/3$, (iv) $t = \pi$, (v) $t = 4\pi/3$, and (vi) $t = 5\pi/3$ are the different phases of the wake behavior.

11 July 2024 03:57:19

Published under an exclusive license by AIP Publishing

their vortices is significantly stronger than modes 3 and 4. The vorticity contours in modes 1 and 2, characterized by opposite signs, are arranged alternately in the streamwise direction, reflecting the convection of the vortices. Similar observations can also be made on the SS cylinder and the OMS cylinder at $f^*_{\mathrm{osc}} = 2$. The vorticity distribution in mode 3 (RC cylinder) is symmetrical about the centerline ($y^* = 0$) and thus reflects the asymmetrical vortex shedding. This asymmetrical behavior is more obvious for the OMS cylinder at $f^*_{\mathrm{osc}} = 2$ (mode 3). In addition, coherent flow structures can be found in the wake of the RC cylinder for the first three POD modes, while only the first two POD modes show apparent coherent flow structures for the SS cylinder and the OMS cylinder at $f^*_{\mathrm{osc}} = 2$. The incoherent flow behavior is more obvious for the OMS cylinder at $f^*_{\mathrm{osc}} = 2$ in modes 3 and 4, which means the oscillatory morphing surface may reduce the flow coherence. Another observation is that the occurrence of vorticity peaks is shifted upstream for the OMS cylinder at $f^*_{\mathrm{osc}} = 2$, aligning with the shorter vortex formation length.

Figure 13 compares the phase-averaged wakes at six phases, i.e., $t = 0$ to $5\pi/3$ with a $\pi/3$ interval, which are determined through the POD analysis. About 350 images (corresponding to $\pm\pi/72$ phase bin size) are used to calculate the mean results at each phase. For the RC cylinder, positive- and negative-signed vortices are alternatively shed from the cylinder, forming a classical von Karman vortex street [see Fig. 13(a)]. The wakes of the SS and RC cases are also similar. However, unlike the apparent rolling-up of the shear layers observed in the RC case, the shear layers behind the SS cylinder are almost parallel at the beginning, then gradually roll up in the far wake, as shown in Fig. 13(b). This is because the flow separation occurs early for the special geometric characteristics of the SS cylinder.

For the dynamic morphing cases, the oscillation of the morphing surface affects the instability of the shear layers and thus changes the subsequent vortex-shedding behavior. For the OMS cylinder at $f^*_{\mathrm{osc}} = 2$, the shear layers roll up early due to the increased instability, as shown in Fig. 13(c). As such, a shorter recirculation region forms. This observation is consistent with the instantaneous flow structures presented in Fig. 3. Differently, phase-averaged results help to focus on the dominant flow structure and show that the von Karman vortex shedding has not been changed for the OMS cylinder at $f^*_{\mathrm{osc}} = 2$, confirming the results found in Fig. 5. More importantly, the location of the first two positive and negative vortices in this case is closer to cylinder, and the distance between these vortices is smaller than the RC and SS cylinders, leading to the higher turbulence intensity in the near wake of the cylinder [Fig. 13(c)]. This explains the results found in Figs. 9 and 10. Moreover, the strength of the vortices in this case is relatively weaker than that of the RC and SS cylinders, which is consistent with that revealed in Fig. 6.

IV. CONCLUSIONS

Based on experimental measurements, the effects of oscillatory morphing surface on cylinder wakes were investigated. This investigation leads to the following conclusions:

(1) Compared with the RC and SS cylinders, the OMS cylinders are able to reduce their vortex formation length, especially for $f^*_{\mathrm{osc}} = 2$, which can achieve a reduction of about 25.2%, with the largest u_{rms} and v_{rms} in the near wake. In addition, the OMS cylinder at $f^*_{\mathrm{osc}} = 2$ can best suppress the strength of time-averaged vorticity and local maximum vorticity.

(2) The oscillatory morphing surface can manipulate the wake structure. Phase-averaged and instantaneous results show that the oscillatory morphing surface can affect the instability of the shear layers. For a lower-frequency perturbation case (e.g., OMS cylinder at $f^*_{\mathrm{osc}} = 1$), the instability of the shear layers is only slightly enhanced. The vortex-shedding behavior is not significantly changed when the excitation frequency is close to the natural vortex-shedding frequency.

(3) For the OMS cylinder operating at $f^*_{\mathrm{osc}} = 2$ and 4, an extra PSD component corresponding to the excitation frequency can be clearly detected. The flow instability is significantly increased owing to the intensive interaction of the morphing surfaces with the shear layers. As such, the shear layers will transition and roll up earlier with a shorter vortex formation length.

(4) When the excitation frequency is remarkably higher than the dominant vortex shedding frequency, i.e., the OMS cylinder at $f^*_{\mathrm{osc}} = 8$, the shear layers are broken up. Interestingly, a train of small vortices will form. They follow the trace of the primary shear layers and roll up into a relatively large vortex.

Although the dynamic surface morphing method can achieve wake control, the current setting did not achieve drag reduction mainly due to the limited operational range of the oscillatory morphing. We are in the process of improving the setup to explore possible drag reduction cases in a larger parameter space. In the future work, we will also explore the performance of partially oscillatory morphing surfaces in wake and drag control.

ACKNOWLEDGMENTS

This study was financially supported by the Research Grants Council of Hong Kong under General Research Fund (Project No. 15218421); L.Z. would like to acknowledge the financial support provided by The Hong Kong Polytechnic University through Research Student Attachment Program. T.H.N. acknowledges the support from the School of Mechanical and Aerospace Engineering, Nanyang Technological University, Singapore.

AUTHOR DECLARATIONS

Conflict of Interest

The authors have no conflicts to disclose.

Author Contributions

Lingwei Zeng: Data curation (equal); Formal analysis (equal); Investigation (equal); Methodology (equal); Software (equal); Writing – original draft (equal); Writing – review & editing (equal). **T. H. New:** Funding acquisition (equal); Project administration (equal); Resources (equal); Supervision (equal); Writing – original draft (equal); Writing – review & editing (equal). **Hui Tang:** Conceptualization (equal); Funding acquisition (equal); Project administration (equal); Resources (equal); Supervision (equal); Writing – original draft (equal); Writing – review & editing (equal).

DATA AVAILABILITY

The data that support the findings of this study are available from the corresponding authors upon reasonable request.

11 July 2024 03:57:19

Published under an exclusive license by AIP Publishing

REFERENCES

[1] C. H. K. Williamson, "Vortex dynamics in the cylinder wake," Annu. Rev. Fluid Mech. **28**, 477–539 (1996).

[2] J. H. Oertel, "Wakes behind blunt bodies," Annu. Rev. Fluid Mech. **22**(1), 539–562 (1990).

[3] Z. Liu, L. Zhou, H. Tang *et al.*, "Primary instability, sensitivity and active control of flow past two tandem circular cylinders," Ocean Eng. **294**, 116863 (2024).

[4] H. Choi, W. Jeon, and J. Kim, "Control of flow over a bluff body," Annu. Rev. Fluid Mech. **40**, 113–139 (2008).

[5] L. Zeng, F. Zhao, H. Wang *et al.*, "A bi-directional flow-energy harvester," Appl. Phys. Lett. **122**, 153901 (2023).

[6] L. Zeng, F. Zhao, H. Wang *et al.*, "Control of flow-induced vibration of a circular cylinder using a splitter plate," Phys. Fluids **35**, 087104 (2023).

[7] F. Zhao, L. Zeng, Z. Wang *et al.*, "Effects of superhydrophobicity on VIV control of a circular cylinder," Appl. Phys. Lett. **123**(10), 101603 (2023).

[8] C. Wang, H. Tang, F. Duan *et al.*, "Control of wakes and vortex-induced vibrations of a single circular cylinder using synthetic jets," J. Fluids Struct. **60**, 160–179 (2016).

[9] H. Tang, P. Salunkhe, Y. Zheng *et al.*, "On the use of synthetic jet actuator arrays for active flow separation control," Exp. Therm. Fluid Sci. **57**, 1–10 (2014).

[10] H. Wang, C. Zhao, L. Zeng *et al.*, "Control of the flow around a finite square cylinder with a flexible plate attached at the free end," Phys. Fluids **34**(2), 27109 (2022).

[11] C. Wang, H. Tang, S. Yu *et al.*, "Active control of vortex-induced vibrations of a circular cylinder using windward-suction-leeward-blowing actuation," Phys. Fluids **28**(5), 53601 (2016).

[12] T. H. New and J. Long, "Dynamics of laminar circular jet impingement upon convex cylinders," Phys. Fluids **27**(2), 24109 (2015).

[13] J. Zhu, H. Wang, and L. Zeng, "Control of the flow around a finite-height square cylinder with slot blowing near its free-end side edges," Phys. Fluids **36**, 025146 (2024).

[14] Q. Zhu, L. Zhou, J. Wen *et al.*, "Laminar flow over a rectangular cylinder experiencing torsional flutter: Dynamic response, forces and coherence modes," Phys. Fluids **35**, 093610 (2023).

[15] D. M. Bushnell and K. J. Moore, "Drag reduction in nature," Annu. Rev. Fluid Mech. **23**(1), 65–79 (1991).

[16] W. Wang, B. Song, Z. Mao *et al.*, "Numerical investigation on vortex-induced vibration of bluff bodies with different rear edges," Ocean Eng. **197**, 106871 (2020).

[17] A. M. El-Makdah and G. F. Oweis, "The flow past a cactus-inspired grooved cylinder," Exp. Fluids **54**(2), 1464 (2013).

[18] Y. Liu, L. Shi, and J. Yu, "TR-PIV measurement of the wake behind a grooved cylinder at low Reynolds number," J. Fluids Struct. **27**(3), 394–407 (2011).

[19] P. Babu and K. Mahesh, "Aerodynamic loads on cactus-shaped cylinders at low Reynolds numbers," Phys. Fluids **20**(3), 35112 (2008).

[20] S. Talley, G. Iaccarino, G. Mungal *et al.*, *An Experimental and Computational Investigation of Flow Past Cacti* (Center for Turbulence Research, NASA Ames/Stanford University, 2001), pp. 51–63.

[21] E. A. Pierson and R. M. Turner, "An 85-year study of saguaro (*Carnegiea gigantea*) demography," Ecology **79**(8), 2676–2693 (1998).

[22] S. Wang, Y. Liu, and Q. Zhang, "Measurement of flow around a cactus-analogue grooved cylinder at $\mathrm{Re_D} = 5.4\times 10^4$: Wall-pressure fluctuations and flow pattern," J. Fluids Struct. **50**, 120–136 (2014).

[23] M. Guttag and P. M. Reis, "Active aerodynamic drag reduction on morphable cylinders," Phys. Rev. Fluids **2**(12), 123903 (2017).

[24] X. Wen, H. Tang, and F. Duan, "Interaction of in-line twin synthetic jets with a separated flow," Phys. Fluids **28**(4), 43602 (2016).

[25] Z. Wei, T. H. New, L. Lian *et al.*, "Leading-edge tubercles delay flow separation for a tapered swept-back wing at very low Reynolds number," Ocean Eng. **181**, 173–184 (2019).

[26] J. H. Lienhard, *Synopsis of Lift, Drag, and Vortex Frequency Data for Rigid Circular Cylinders* (Technical Extension Service, Washington State University, Pullman, WA, 1966).

[27] J. H. Gerrard, "The mechanics of the formation region of vortices behind bluff bodies," J. Fluid Mech. **25**(2), 401–413 (1966).

[28] W. Thielicke and R. Sonntag, "Particle image velocimetry for MATLAB: Accuracy and enhanced algorithms in PIVlab," J. Open Res. Softw. **9**(1), 12 (2021).

[29] T. H. New, S. Shi, and B. Zang, "Some observations on vortex-ring collisions upon inclined surfaces," Exp. Fluids **57**(6), 109 (2016).

[30] T. H. New, J. Long, B. Zang *et al.*, "Collision of vortex rings upon V-walls," J. Fluid Mech. **899**, A2 (2020).

[31] T. H. New and B. Zang, "Head-on collisions of vortex rings upon round cylinders," J. Fluid Mech. **833**, 648–676 (2017).

[32] C. Zhao, H. Wang, L. Zeng *et al.*, "Effects of oncoming flow turbulence on the near wake and forces of a 3D square cylinder," J. Wind Eng. Ind. Aerodyn. **214**, 104674 (2021).

[33] T. H. New, S. Shi, and Y. Liu, "On the flow behaviour of confined finite-length wavy cylinders," J. Fluids Struct. **54**, 281–296 (2015).

[34] T. H. New, S. Shi, and Y. Liu, "Cylinder-wall interference effects on finite-length wavy cylinders at subcritical Reynolds number flows," Exp. Fluids **54**(10), 1601 (2013).

[35] K. E. Meyer, J. M. Pedersen, and O. Özcan, "A turbulent jet in crossflow analysed with proper orthogonal decomposition," J. Fluid Mech. **583**, 199–227 (2007).

[36] L. Ma and L. Feng, "Experimental investigation on control of vortex shedding mode of a circular cylinder using synthetic jets placed at stagnation points," Sci. China Technol. Sci. **56**, 158–170 (2013).

[37] N. Kim, H. Kim, and H. Park, "An experimental study on the effects of rough hydrophobic surfaces on the flow around a circular cylinder," Phys. Fluids **27**(8), 85113 (2015).

[38] C. Wang, H. Tang, S. Yu *et al.*, "Lock-on of vortex shedding to a pair of synthetic jets with phase difference," Phys. Rev. Fluids **2**(10), 104701 (2017).

[39] C. Norberg, "LDV-measurements in the near wake of a circular cylinder," in *Proceedings of the 1998 ASME Fluids Engineering Division Summer Meeting* (ASME, Washington, DC, 1998).

[40] L. Sirovich, "Turbulence and the dynamics of coherent structures. I. Coherent structures," Q. Appl. Math. **45**(3), 561–571 (1987).

[41] B. W. van Oudheusden, F. Scarano, N. P. van Hinsberg *et al.*, "Phase-resolved characterization of vortex shedding in the near wake of a square-section cylinder at incidence," Exp. Fluids **39**, 86–98 (2005).

11 July 2024 03:57:19

Published under an exclusive license by AIP Publishing